PAPER

Texturing of pure and doped CeO$_2$ thin films by EBPVD through target engineering†

P. Arunkumar,[a] R. Ramaseshan,*[b] S. Dash,[b] Joysurya Basu,[b] T. R. Ravindran,[b] S. Balakumar[c] and K. Suresh Babu*[a]

In this paper, we report the effect of annealing temperature of target on the texture of thin films coated by electron beam physical vapor deposition method. Nanocrystalline cerium oxide (CeO$_2$) and 20 mol% samarium doped cerium oxide (SDC) powders, compacted into pellets, were used as targets after annealing at 300, 500 and 800 °C. Grain size analysis of the target by X-ray diffraction showed a size range of 12–52 nm and 9–22 nm for CeO$_2$ and SDC, respectively. Texture coefficient calculation from glancing incident X-ray diffraction showed a preferential orientation of (111) in CeO$_2$ films. However SDC films exhibited (200) orientation grown at the expense of (111) which resulted in higher residual strain with annealing temperature. The pole figure analysis elucidated smaller in-plane misorientation in CeO$_2$ than in SDC films. Under similar deposition conditions, difference in textured growth between CeO$_2$ and SDC is primarily induced by vapor pressure modifications associated with the annealing temperature of the target. Raman and X-ray photoelectron spectroscopic studies of the films indicate the presence of higher oxygen vacancy concentration in SDC as well as a decrease in Ce^{3+} concentration with target annealing temperature.

1 Introduction

Solid oxide fuel cells (SOFCs) are potential devices for efficient electric power generation due to lower pollution and fuel flexibility *etc.* The commercialization of SOFCs is limited due to high operating temperature (1000 °C) required for sufficient energy generation.[1] Among all the components, electrolyte material property plays an important role for the migration of oxygen ions through electrolyte thereby deciding the operating temperature of SOFC. Cerium oxide (CeO$_2$) based materials are widely used as electrolyte for intermediate temperature operations.[2] Cerium in CeO$_{2-\delta}$, exists in two oxidation states (namely +3 and +4) and changes the oxidation state in response to the external environment or with intrinsic changes in stoichiometry.[3] Doping with tri- or di-valent dopant in cerium oxide creates the oxygen vacancy inside the lattice for charge neutrality. Increase in oxygen vacancy inside the fluorite lattice of CeO$_2$ facilitates the diffusion of oxygen ions at reduced activation energy and increases the ionic conductivity at a given temperature.[2] At intermediate operating temperature (600 °C), doped CeO$_2$ exhibits higher ionic conductivity compared to that of conventional stabilized zirconia.[4] Samarium doped cerium oxide is reported as one among the potential electrolyte materials for intermediate temperature solid oxide fuel cell (ITSOFC) applications. Doping Sm^{3+} in CeO$_2$ increases the ionic conductivity by reducing the migration enthalpy of oxygen ion inside the lattice and improves the stability against the reducing environment in low oxygen partial pressure conditions.[5-8] Fabrication of electrolyte in the form of thin films reduces the overall ohmic polarization loss as well as eliminates the process of sintering and thereby lowering the operating temperature while retaining the nanocrystallinity of the material.[9] Grain boundaries require higher activation energy for oxygen ion conduction in micron sized particles whereas in nanomaterial lower activation energy makes it a conduction path leading to super ionic conductivity.[10] As a result one can expect nanomaterial based thin film electrolyte to show reduced activation energy for ionic conductivity. Thus there is a renewed research interest in the field of thin film based ionic devices which will facilitate the miniaturization of energy conversion devices.

For the fabrication of SOFC thin films both physical vapour deposition (PVD)[11] and wet chemical synthesis[12] are being explored. However, PVD techniques enable the formation of dense thin film coatings with controllable thickness and crystallite quality in the nano regime.[13] Electron beam deposition (EBPVD),[14] pulsed laser deposition,[15] sputtering[16] and chemical vapour deposition[17] are widely used techniques for the

[a]Centre for Nanoscience and Technology, Madanjeet School of Green Energy Technologies, Pondicherry University, Puducherry – 605 014, India. E-mail: sureshbabu.nst@pondiuni.edu.in

[b]Indira Gandhi Centre for Atomic Research, Kalpakkam – 603 102, India. E-mail: seshan@igcar.gov.in

[c]National Centre for Nanoscience and Nanotechnology, University of Madras, Guindy Campus, Chennai- 600 025, India

† Electronic supplementary information (ESI) available. See DOI: 10.1039/c4ra04353g

fabrication of SOFCs. In the electron beam evaporation technique, the deposition of the films is carried out under high vacuum conditions with variable substrate temperature and with controlled epitaxial growth. The conductivity of CeO_2 based electrolyte coating is sensitive to the morphology of the thin films as it affects the oxygen vacancy and Ce^{3+} concentration inside the lattice.[18] The crystallographic anisotropy of ion conduction in polycrystalline thin films is partly bypassed in textured thin films. The anisotropic nature of thin film is more for polycrystalline film compared to the textured film, in turn texturing enhances the conductivity through ordered pathway of ionic conduction.[19,20] In general, the texture in thin films is introduced either by depositing the film on the textured substrate or by tuning the deposition parameters such as substrate temperature,[21] deposition rate[22] and oxygen partial pressure.[12]

Usually for the deposition of films from powder, a pellet is made and placed in the electron beam hearth. The other deposition parameters such as partial pressure, substrate temperature, power *etc.* are tuned in order to deposit films of specific nature. However, our interest is in investigating/ understanding the effect of heat treatment to the target before evaporation on the subsequent characteristics of thin films such as grain size, stoichiometry defect size, *etc.* Therefore, the powder was compacted and subjected to heat treatment at 300, 500 and 800 °C. To the best of our knowledge, so far the correlation of target material properties with preferential orientation of the resultant thin film in CeO_2 based systems have not been studied. In the present work we report the effect of target condition in electron beam evaporation process on the texture quality of deposited CeO_2 and samarium doped CeO_2 thin films.

2   Experimental detail

CeO_2 and 20 mol% of samarium doped CeO_2 (SDC) were prepared by co-precipitation method. Cerium nitrate hexahydrate (Ce $(NO_3)_3 \cdot 6H_2O$, Sigma-Aldrich, 99%), samarium nitrate hexahydrate (Sm $(NO_3)_3 \cdot 6H_2O$, Alfa-Aesar, 99.9%) were used as metal precursors and ammonium hydroxide as precipitating agent. Cerium nitrate (0.05 M) dissolved in 100 ml of deionized water was precipitated using ammonium hydroxide solution (pH ∼ 10) under constant stirring at room temperature for 4 hours which results in pale yellow coloured CeO_2 precipitate. For the preparation of SDC, aqueous solutions of cerium nitrate hexahydrate and samarium nitrate hexahydrate were mixed together in stoichiometric proportions and precipitated by aqueous ammonium hydroxide solution. The resultant precipitates were washed and dried at 100 °C overnight to obtain CeO_2 and SDC powders. As prepared CeO_2 and SDC powders were compacted into pellets (10 mm diameter × 2 mm thickness) in an automatic uniaxial isostatic press at 5 tons of pressure. These pellets were annealed at 300, 500 and 800 °C for 4 hours in order to understand the effect of annealing. As compacted (RT) and annealed pellets were used as target materials for e-beam evaporation (BC-300 Vacuum box coater, HINDHIVAC, India). A base pressure of ∼3 × 10^{-6} mbar and a constant power of

0.3 kW were maintained throughout the deposition. During deposition the substrate temperature was maintained at 100 °C and the substrate was kept at a distance of 250 mm away from the target. Thin films were grown on glass substrates with a uniform thickness of 200 nm which was confirmed by profilometer (Dektak 6, Veeco, USA).

The crystallographic phase of the target was studied using X-ray diffraction (XRD) analysis (Ultima IV, Rigaku, Japan). The XRD pattern was recorded with a step size of 0.02° with monochromatic Cu Kα radiation. The mean crystallite size was calculated by Scherrer formula. Williamson–Hall method was used to calculate strain of the CeO_2 and SDC pellets using the eqn (1).

$$\beta \cos \theta = \frac{K\lambda}{L} + 4\varepsilon \sin \theta \qquad (1)$$

Where K is the Scherrer constant which is equal to 0.9, L is the crystallite size, θ is the angle, β is the full width half maxima, ε is the associated strain value for corresponding samples. The terms $\beta \cos \theta$ and $4 \sin \theta$ were plotted against each other. Accordingly associated slope and y-intercept from the plot gives the strain (ε) and crystallite size $(K\lambda/L)$ value respectively. The texture quality and phase structure of the thin films were analyzed by glancing incident X-ray diffraction (GIXRD, D8 Advance Bruker, Germany) at an incidence angle of 0.5°. Pole figures (ψ and ϕ scan) were recorded for (111) and (200) planes in both CeO_2 and SDC films in order to understand the texture quality with respect to target annealing temperature. In order to analyze the oxygen vacancy concentration in the target material and in thin films, Raman spectra were recorded using micro Raman spectrometer (Renishaw, UK), with an excitation laser wavelength of 514 nm at room temperature. The ratio of Ce^{3+} to Ce^{4+} concentration was quantified by X-ray photoelectron spectroscopy (XPS) with Al Kα monochromatic X-ray radiation at 300 W using an Omicron nanotechnology. In order to quantify the concentrations of Ce^{3+} and Ce^{4+}, the obtained peaks from XPS were deconvoluted using Peak Fit software version 4.0.

3   Result and discussion

3.1   XRD analysis

Fig. 1(a) shows the Bragg–Brentano (B–B) geometry XRD patterns of the annealed targets. The characteristic peaks of the XRD patterns matches with that of CeO_2 (JCPDS no. 34-0394), which is cubic fluorite in structure.

The average crystallite size of all the samples was calculated from (111), (200), (220) and (311) peaks of XRD using Scherrer's formula. In CeO_2 targets the crystallite size varied from 12 to 52 nm with increase in annealing temperature. The peak broadening of CeO_2 reduces gradually with increase in annealing temperature due to strain relaxation and surface energy minimization driven grain growth. Fig. 2 shows the associated lattice strain calculated from Williamson–Hall method for various targets. As expected, the strain in CeO_2 decreases with increase in annealing temperature indicating a lattice relaxation at higher temperature.
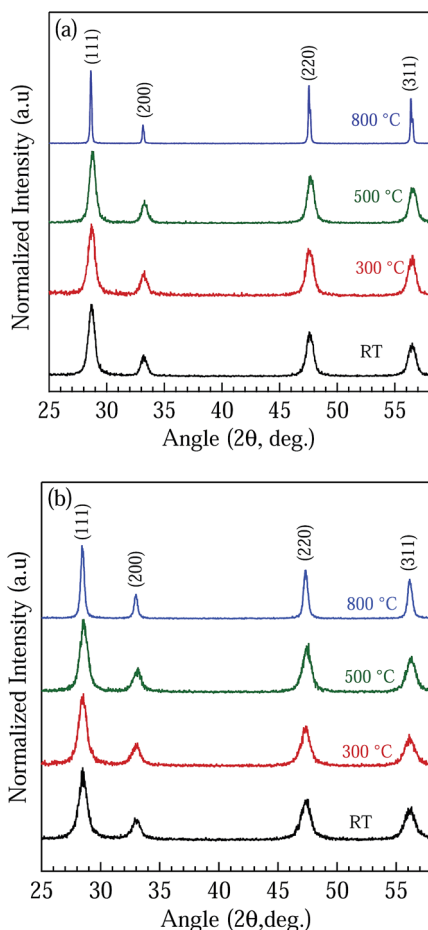
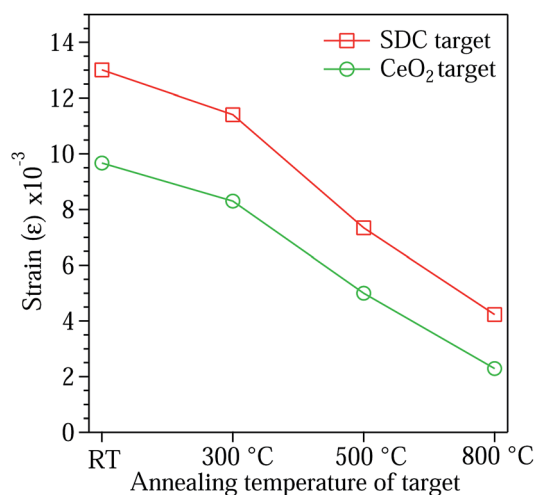**Fig. 1** B–B geometry XRD of (a) CeO$_2$ (b) SDC targets with different annealing temperatures.

Fig. 2 Strain value of CeO$_2$ and SDC target with respect to annealing temperature.

peak for other phase confirms the complete dissolution of samarium in the ceria lattice. In SDC, peak broadening decreases with increase in annealing temperature. The XRD peaks of SDC shift towards lower angle as compared to pure CeO$_2$. This is attributed to the lattice expansion induced by samarium doping. The crystallite size of SDC targets annealed at different temperatures increases from 9 to 22 nm as calculated using the Scherrer's formula. Compared to CeO$_2$, SDC showed a smaller crystallite size, signifying the role of external dopant hindering the nucleation process of the host atom (Ce ion) during the synthesis process.[24] Additionally, doping with samarium changes the surface energies of pure CeO$_2$ which always play a key role in grain growth during sintering.

Fig. 2 shows the strain variation with annealing temperature. Strain value for SDC targets are relatively higher than that of CeO$_2$ due to the substitution of larger Sm^{3+} ions (1.08 Å) in the host lattice of Ce^{4+} ions (0.96 Å). However the strain value for SDC decreases with annealing temperature due to the relaxation of lattice at higher temperatures.[23]

The above characterized targets were used in EBPVD for depositing thin film on the glass substrate. Fig. 3(a) & (b) shows
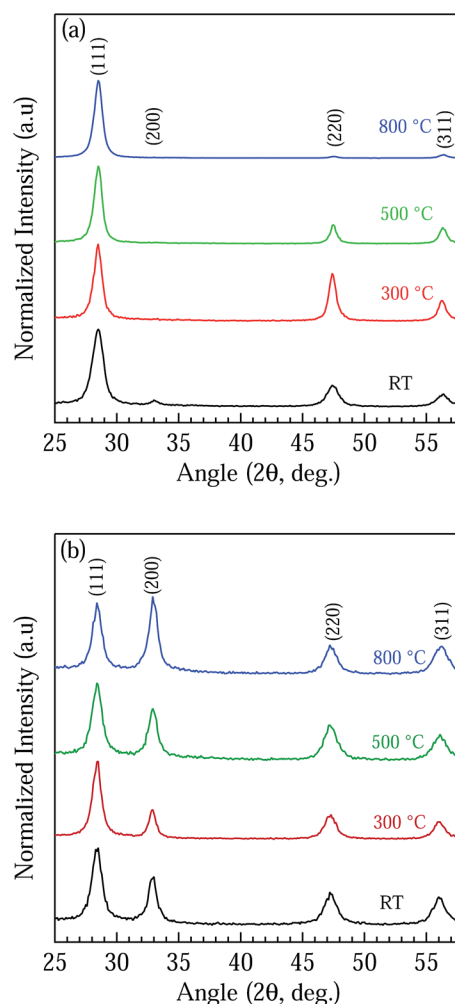

Fig. 3 GIXRD pattern of electron beam deposited thin films (a) CeO$_2$ (b) SDC using various targets.

X-ray diffraction pattern of SDC targets indicate that upon doping samarium, the cubic fluorite structure of CeO$_2$ has been retained as shown in Fig. 1(b). Absence of any characteristics

the GIXRD pattern of CeO_2 and SDC thin films which matches with JCPDS data for CeO_2. However, with increase in the annealing temperature of the target, the (111) grows at the cost of other orientations in CeO_2 thin films. This indicates that with the increase in annealing temperature, the growth of thin films tend to develop the (111) texture. Fig. 3(b), in SDC films the variation of relative intensities of the planes with annealing temperature differs from the observation made in the case of CeO_2. The intensity of the (200) peak of SDC grows significantly with increase in annealing temperature contrary to the growth of (111) plane in CeO_2.

In EBPVD technique, it is expected that the characteristics of the deposited film should not depend on the prior processing history of the target material as it is evaporation and deposition assisted by the electron beam. But in the present case variation in orientation was observed with change in annealing temperature and chemistry of the target. The primary characteristics of the targets that change with annealing temperature is the residual strain and surface faceting. It appears that residual strain and surface faceting of the targets significantly change the evaporation rate that subsequently changes the growth characteristics of the films. Using Scherrer equation the crystallite size of thin films was calculated and the variation found to be minimal in spite of the large variation in crystallite size in targets with annealing temperature. The crystallite size of CeO_2 film was found to be increasing from 7 to 10 nm with annealing temperature of target. However in SDC film the crystallite size varied from 6 to 9 nm with annealing temperature of the target and peaks shifted towards lower angles in comparison to CeO_2 films.

Preferential orientation of thin film can be quantitatively analyzed by determining the texture co-efficient (TC). Harris equation (eqn (2)) was used to calculate the TC for thin films from GIXRD patterns.[25]

$$T_{hkl}(\text{TC}) = \frac{\left(I_{hkl}/I_{hkl}^*\right)}{\left(1/n\Sigma\left[I_{hkl}/I_{hkl}^*\right]\right)} \tag{2}$$

Where I_{hkl} denotes the experimental intensity obtained from XRD peak of particular orientation, I_{hkl}^* denotes the JCPDS intensity of corresponding plane and n is the number of peak used for calculation. Table 1 shows the TC value of CeO_2 and SDC films with respect to the annealing temperature. For polycrystalline thin film the TC is less than or equal to one while for preferentially oriented film the TC value is reported to be more than one. When TC value is greater than one, large

proportion of grains are progressively orienting towards a particular plane.[26,27]

The TC from Table 1 shows the transition of polycrystalline film towards particular orientation in both CeO_2 and SDC films with annealing temperature. The TC value for CeO_2 shows the transition from mixed to (111) orientation. In SDC the observed TC value was greater than one for both (111) and (200) plane. With an increase in annealing temperature the TC value for (200) plane increases while a decrease in (111) signifies the preferential orientation of (200). Thus the TC shows a change-over from mixed to particular orientation in these thin films as a function of annealing temperature.

To understand the texture quality of the thin films with respect to the annealing temperature of the target, pole figure analysis was carried out. For pole figure analysis only (111) plane of CeO_2 (500, 800 °C) and for SDC (111) & (200) planes were taken into consideration in order to analyze the texture quality of both CeO_2 and SDC thin films. Pole figure was recorded by fixing the X-ray source and detector on a particular plane with respect to tilt angle (ψ) of sample from 0–90° by rotating the sample (ϕ) from 0–360° at their axis for every 1°.

The contour plot of pole figure analysis in (111) and (200) planes for CeO_2 and SDC are shown in Fig. 4. The GIXRD profiles at $\psi = 0$ clearly show the (111) and (200) planes were preferentially oriented for CeO_2 and SDC thin films, respectively. The concentric circle in contour plot of pole figure refers to the diffraction pattern of a particular plane from the sample. Broader distribution of concentric circles in contour plot indicates the poor texture quality of thin film. However, narrow distribution indicates the high quality of textured film.[24]

In CeO_2 films, the preferential orientation of (111) planes with increase in annealing temperature were confirmed by TC values. The pole figure analysis of (111) planes show the decrease in broadness of concentric circle in contour plot (Fig. 4(a) & (b)) with increase in annealing temperature of target. The broadenings are roughly 11° and 10° respectively for the films grown from the targets annealed at 500 and 800 °C. This out of plane orientation of (111) planes indicate the formation of low- and medium-angle boundaries in the film. As annealing temperature of target increases from 500 to 800 °C, the tilt among the grains remain almost similar. It appears from this study that annealing temperature of the target does not influence significantly to the nature of the grain boundaries for CeO_2. The contour plots of pole figures analysis for both (111) and (200) planes for SDC thin film are shown in the Fig. 4(c)–(f). In the case of SDC, (200) plane tends to orient over the (111) planes as observed from TC value. In SDC films, the misorientation among (111) planes are 29° and 13° for the annealing temperature 500 and 800 °C respectively. However in (200) planes misorientation angles are 39° and 30° for the annealing temperature 500 and 800 °C, respectively. It appears that the maximum misorientation angle among the grains with respect to (111) and (200) planes are significantly higher in the case of SDC than in CeO_2. It is understood that due to the texturing competition among (111) and (200) planes in SDC, the misorientation angles are higher.

Table 1 Texture co-efficient calculated using Harrish equation from GIXRD pattern for CeO_2 and SDC

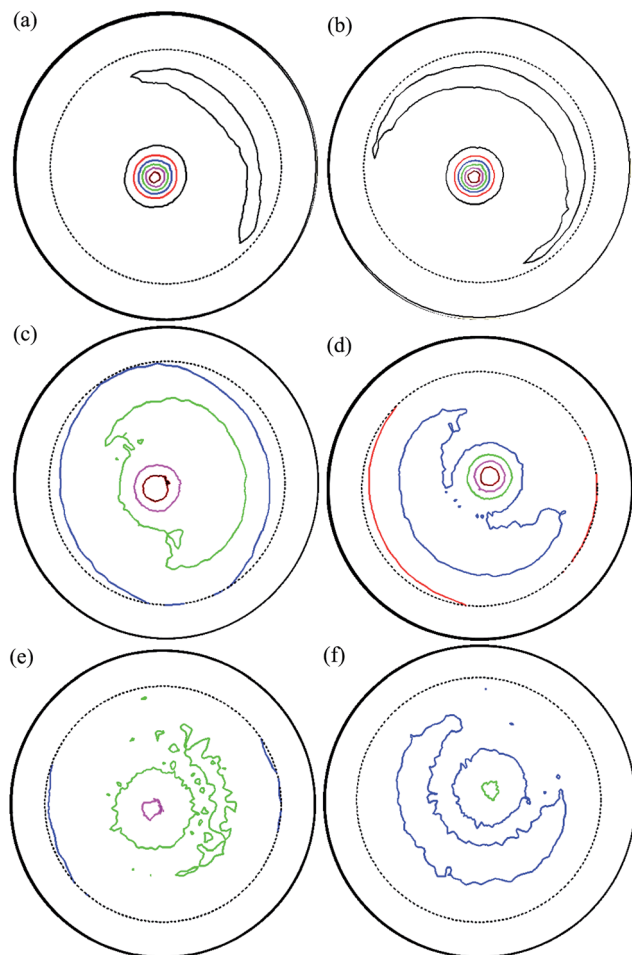| Plane	Texture coefficient of CeO_2				Texture coefficient of SDC			
	RT	300 °C	500 °C	800 °C	RT	300 °C	500 °C	800 °C
(111)	2.25	2.64	2.94	3.7	1.3	1	0.95	0.68
(200)	0.52	0	0	0	1.55	1.84	1.95	2.45
(220)	0.64	0.72	0.41	0.08	0.56	0.60	0.60	0.39
(311)	0.47	0.63	0.64	0.20	0.59	0.48	0.48	0.46

Fig. 4 Contour plots of CeO_2 thin films (111) orientation grown at the temperature (a) 500 °C (b) 800 °C and contour plot of SDC thin films (111) orientation grown at the temperature (c) 500 °C (e) 800 °C, (200) orientation (d) 500 °C (f) 800 °C.
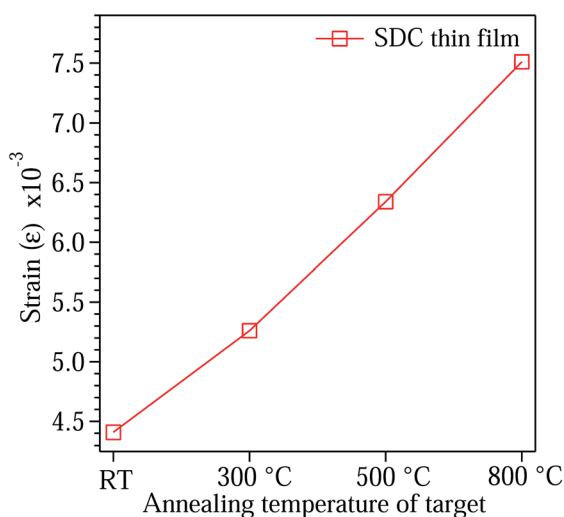

Fig. 5 Strain value calculated for SDC thin film using Williamson Hall plot method.

The lattice strain of the SDC thin films was determined using Williamson–Hall method as shown in the Fig. 5. Interestingly residual strain in SDC film increases with increase in the annealing temperature which is opposite to that of observed in targets. Although, pole figure analysis (Fig. 4) indicates that the annealing temperature does not significantly influence the grain boundary structure, however, with an increase in annealing temperature (200) grows at the expense of (111). Due to this competition, misfit strain may be introduced among the grains which are reflected in the residual strain analysis (Fig. 5). The similar strain analysis for CeO_2 thin films was not possible as single (111) orientation dominates with annealing temperature. The residual strain for SDC thin films is found to be higher when compared to that of targets. This observation could be attributed to the interfacial mismatch strain between the coating and the substrate. Moreover, immediate condensation of the coating over the substrate during deposition may also contribute towards the higher residual strain that is observed in the coating. It is worth mentioning that although the deposition parameters are identical, the target annealed at 800 °C is more strain relaxed. As a result evaporation rate from the target is different which is leading to the development of (200) texture simultaneously with (111) texture. In thin films, major sources of residual strains are film–substrate interface and the grain boundaries. As in the SDC film (200) texture are developing along with (111), it generates more interfaces and thus more residual strain. This could be the reason for the observed higher residual strain in the films deposited from 800 °C annealing. Generally the strain energy increases with decrease in planar density along the crystallographic planes in the order of (111) < (220) < (200).[25] The TC value (Table 1) and pole figure of SDC film clearly indicates the emergence of (200) plane at the cost of (111) with annealing temperature. Thus the preferred orientation of the (200) plane in turn increases the lattice strain as supported by stain curve with respects to temperature (Fig. 5).

3.2 Growth mechanism in textuted film

In physical vapor deposition process (PVD) such as EBPVD, the orientation of the thin film is affected by the process parameters such as substrate temperature, deposition rate, residual gas pressure and thickness of the film. Any variation in the above parameters would influence the migration energy of the adatom on the substrate during the growth process of the thin film.[28] At the initial stage when the adatom arrives on the glass substrate, limited migration results in the nucleation to form island. Further arrival of adatom on the island results in increased migration energy of deposited atom. The increase in migration energy tends to facilitate the migration of the adatom from the deposited place to several angstroms in order to attain the thermodynamically stable state by minimizing the surface and interfacial energy. Furthermore, the presence of dopant elements disturbs the thermodynamically stable state of the host atom as suggested by Dutta and Williams (DW).[28]

The surface stability of CeO_2 (FCC) follow the tendency in the order of (111) > (200) > (220).[29] In this present work since all e-beam parameters were kept constant, the only change in the

annealing temperature of target led to the preferential orientation of (111) plane in CeO$_2$ and (200) plane in SDC. It is worthy to mention that the target compacted at room temperature has relatively finer grain size and more surface area compared to that of annealed targets at higher temperature where grains are grown and their less energy facets are exposed. Hence under similar electron beam deposition conditions evaporating the atoms of as prepared target is easier as compared to that of annealed ones. Therefore increase in annealing temperature of the target material in turn decrease the vapor stream of the evaporated cluster.[30,31] Hence the proportion of atoms reaching the substrate at a given time varies with respect to crystallinity of the material.

Evaporation of room temperature target material results in an increased number of atoms arriving the substrate. According to DW growth mechanism, increase in the arrival rate of adatoms to the substrate, in turn traps the mobility of atom which results in a polycrystalline thin film. However increase in annealing temperature of the target decreases the number of adatoms arriving at the substrate. This results in enough mobility of the atoms and extends the opportunity for the atom to reach the minimum energy configuration. Therefore in CeO$_2$ the TC value of (111) plane increases with increase in annealing temperature of the target. Hence in CeO$_2$ thermodynamically favorable (111) shows the preferential orientation.

In the case of SDC thin film, (200) plane grows at the cost of (111) with increase in annealing temperature of the target as evident from pole figure analysis and TC values. In SDC thin film according to DW growth mechanism, the presence of foreign atom (Sm) hinders the mobility of host atom (Ce). Generally the Ce atom tries to move towards lower surface energy plane of (111), but due to the disturbance in mobility by Sm atom in SDC film, the Ce atom tries to stabilize itself to the next possible energy state. Basu et al., experimentally proved that the surface energy of both (111) and (100) are close to each other for trivalent doped CeO$_2$.[32] Hence thermodynamically the disturbance in mobility of Ce atom in SDC leads to the orientation of (200) plane which is energetically close to the (111) plane. The above discussion clearly shows that the properties of initial target material have strong influence on orientation of the thin film.

3.3 Defect chemistry

The electrolyte property of thin film based ITSOFC is strongly influenced by the orientation of thin film. Decrease in activation energy was observed in preferentially oriented thin film compared to that of random orientation.[33] Additionally the activation energy also depends on the oxygen vacancy and Ce^{3+} concentration (intrinsic property) of thin film. Hence Raman spectroscopy and XPS studies were carried out in order to understand the modification of defect chemistry upon deposition with respect to the annealing temperature of target.

The Raman spectra for both targets and thin films are shown in Fig. 6. Raman spectra of CeO$_2$ consist of intense band at 465 cm^{-1} (Fig. 6), which corresponds to F$_{2g}$ vibrational mode of Ce–O8.[34] The observed additional weak peak at 600 cm^{-1} in
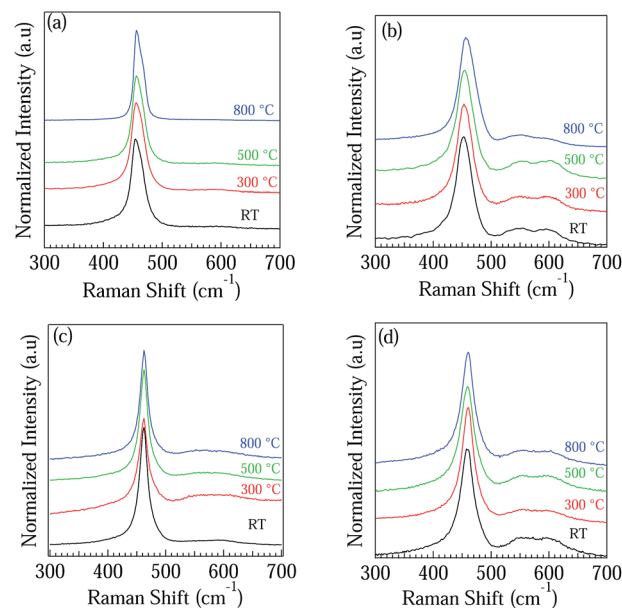

Fig. 6 Raman spectra for target (a) CeO$_2$ (b) SDC as well as thin films of (c) CeO$_2$ (d) SDC.

CeO$_2$ (target & thin film) can be attributed to oxygen vacancies created by the Ce^{3+} concentration inside the lattice.[36] The Raman peak position shift towards higher energy with increase in the annealing temperature (Fig. 7) was due to the strain relaxation and increase in crystallite size.[35] Thin film also exhibits a similar trend of peak shift as that of target. It is understood that the annealed targets provide enough migration time for the adatom compared to as prepared targets (RT), which in turn helps the growth of thin film with minimum lattice distortion. By doping Sm^{3+} in CeO$_2$, the Raman peak shifts towards lower energy for both the target and the thin film, signifying the lattice expansion induced by the dopant in the host lattice.
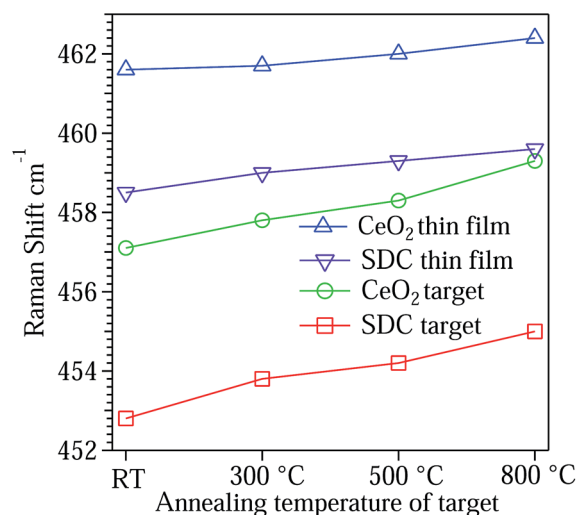

Fig. 7 Raman peak shift for target and thin films.

Additionally two weak peaks at 550 and 600 cm^{-1} have been observed for SDC in the target as well as in the thin films. These bands at 550 and 600 cm^{-1} correspond to the oxygen vacancies created by Sm^{3+} doping and Ce^{3+} inside the lattice. Annealing enriches the oxidation of Ce^{3+} to Ce^{4+}, thus the reduction in intensity of the peak at 600 cm^{-1} was observed for SDC target (Fig. 6(b)). Reduction in intensity at 600 cm^{-1} was also observed for thin films (Fig. 6(c)) indicating the influence of target material properties on the deposition of thin films. The presence of Sm^{3+} and Ce^{3+} inside the CeO$_2$ lattice creates oxygen vacancy in order to maintain charge neutrality.[37] Doping of trivalent element (Sm^{3+}) inside the crystal lattice of CeO$_2$ creates oxygen vacancies as in the eqn (3).

$$Sm_2O_3 \xrightarrow{CeO_2} 2Sm'_{Ce} + 3O^{\times}_O + V^{..}_O \qquad (3)$$
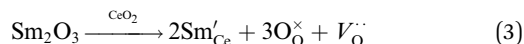
The strong F$_{2g}$ band at 465 cm^{-1} corresponds the vibrational mode of Ce–O8, thus this mode is very sensitive to the lattice distortion caused by the absence of oxygen inside the cubic fluorite structure of CeO$_2$. Therefore increase in non-stoichiometry of CeO$_2$ induces a broadening effect and asymmetry nature of F$_{2g}$ mode vibration.[38] The asymmetric nature of major peak at ∼465 cm^{-1} was used to calculate the concentration of oxygen vacancy using spatial correlation model.[39]

$$N = \frac{3}{4\pi L^3} \qquad (4)$$

Where N is the defect concentration and L is the correlation length between two defect present inside the lattice. Fig. 8 shows the oxygen vacancy concentration calculated from the eqn (4). SDC shows increased oxygen vacancy compared to that of CeO$_2$ in both target and thin film. For CeO$_2$ target, the oxygen vacancy concentration decreases with annealing temperature due to the re-oxidation process of Ce^{3+} to Ce^{4+}.

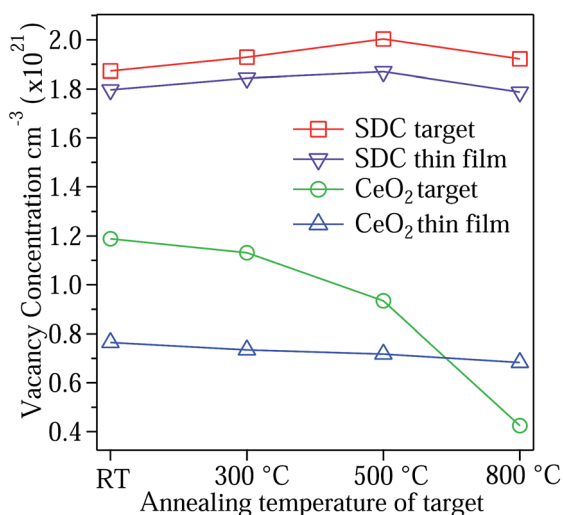The oxygen vacancy concentration is more for powder than in thin films, due to the scaling down process of thin film.

Therefore minimum changes of oxygen vacancy concentration were observed in thin film with respect to annealing temperature. Thus Raman spectroscopic study helps to understand the influence of initial material property on thin film.

The XPS spectrum of Ce (3d) region (Fig. 9) was measured in thin films, in order to analyze the surface concentration of Ce^{3+}. The XPS spectrum were charge corrected using 1s carbon at 284.6 eV as reference peak. The Ce (3d) spectrum is a combination of both Ce^{3+} and Ce^{4+} oxidation state and exhibits multiple peak due to splitting of spin doublets (3d$_{3/2}$ and 3d$_{5/2}$ orbit). In order to separate the contribution of dual oxidation states, the peaks were deconvoluted using Peak fit programme.
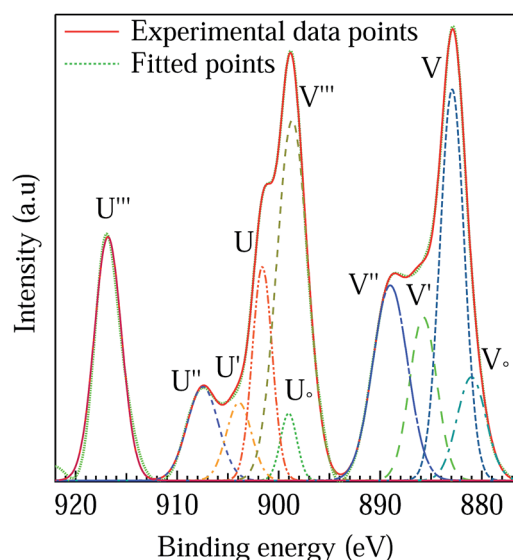

Fig. 9 Representative XPS spectrum of CeO$_2$ thin film deposited from 800 °C annealed target showing deconvoluted peaks. Solid lines represent the experimental data while the dotted lines represents the fit for the deconvoluted peaks.
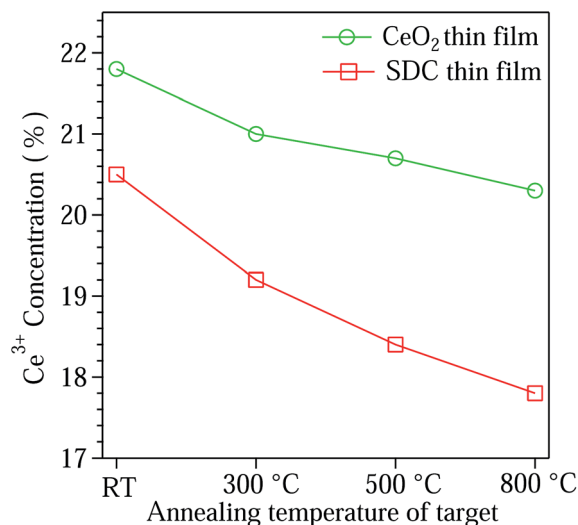

Fig. 8 Oxygen vacancy concentration calculated using spatial correlation model for various targets and thin films.

Fig. 10 Ce^{3+} concentration calculated from XPS analysis for deposited thin films.

The deconvoluted peaks of v^o, v' u^o, u' and v, v'', v''', u, u'', u''' are attributed to the Ce^{3+} and Ce^{4+} oxidation states respectively.[40] The area under the deconvoluted peaks were used to calculate the Ce^{3+} concentration using the eqn (5)

$$Ce^{3+} = \frac{A_{v^o} + A_{v'} + A_{u^o} + A_{u'}}{A_v + A_{v''} + A_{v'''} + A_u + A_{u''} + A_{u'''} + A_{v^o} + A_{v'} + A_{u^o} + A_{u'}} \quad (5)$$

A_i indicates the integrated area of respective deconvoluted peak i. Fig. 10 shows the SDC thin film with minimum concentration of Ce^{3+} compared to that of CeO_2, indicates that doping Sm^{3+} minimizes the formation of Ce^{3+}. The analysis of XPS spectra (Fig. 10) shows that the concentration of Ce^{3+} decreases for the thin film with respect to annealing temperature. The XPS results of Ce^{3+} concentration, supports the oxygen vacancy concentration calculated from Raman spectra (Fig. 8). XPS results which is more sensitive to the surface supports that the initial vacancy concentration in target gets reflected on the deposited thin film.

4 Conclusion

The texture quality and defect chemistry of thin film deposited using EBPVD has been studied in detail with respect to the annealing temperature of target. Increase in annealing temperature of target grows the intensity of (111) and (200) planes of CeO_2 and SDC films, respectively. The TC value for (111) planes in CeO_2 increases with increase in annealing temperature. On the other hand, in SDC thin film (200) planes grow at the cost of (111) planes with annealing temperature. Pole figure analysis in CeO_2 thin film shows that the misorientation angle within the (111) planes. In the case of SDC thin film the misorientation angle is large. It denotes that in SDC the growth competition between (200) and (111) planes exist on epitaxial growth of thin film. For SDC thin film, the increase in strain value with the increase in annealing temperature of target is the reason behind the emergence of (200) plane at the cost of (111). It is understood that the effect of annealing temperature in turn affects the residual strain value of the thin film. Through spatial correlation model the oxygen vacancy was calculated from Raman spectroscopy for both target and thin films. The change in vacancy concentration of both thin film and target material follows the similar trend denoting the effect of target material on deposited thin films. The surface sensitive technique XPS shows the decrease in Ce^{3+} concentration with respect to annealing temperature. Thus the present study demonstrates the effect of change in the properties of target material in tuning the texture and defect chemistry of deposited thin film in electron beam evaporation process which is of importance to tailor oriented thin films. The reported results are likely to provide better insight about electron beam process and orientation of thin films for potential fuel cell applications.

Acknowledgements

References

1 J. Will, A. Mitterdorfer, C. Kleinlogel, D. Perednis and L. J. Gauckler, *Solid State Ionics*, 2002, **131**, 79–96.

2 P. Arunkumar, M. Meena and K. Suresh Babu, *Nanomater. Energy*, 2012, **1**, 288–305.

3 M. Mogensen, N. M. Sammes and G. A. Tompsett, *Solid State Ionics*, 2000, **129**, 63–94.

4 M. L. Faro, D. L. Rosa, V. Antonucci and A. S. Aric, *J. Indian Inst. Sci.*, 2009, **89**, 363–380.

5 H. Yahiro, Y. Eguchi, K. Eguchi and H. Arai, *J. Appl. Electrochem.*, 1988, **18**, 527–531.

6 H. Yahiro, K. Eguchi and H. Arai, *Solid State Ionics*, 1989, **36**, 71–75.

7 S. Zha, C. Xia and G. Meng, *J. Power Sources*, 2003, **115**, 44–48.

8 V. V. Kharton, F. M. B. Marques and A. Atkinson, *Solid State Ionics*, 2004, **174**, 135–149.

9 B. Zhu, *J. Power Sources*, 2003, **114**, 1–9.

10 B. Zhu, C. Xia, X. Luo and G. Niklasson, *Thin Solid Films*, 2001, **385**, 209–214.

11 J. Santiso and M. Burriel, *J. Solid State Electrochem.*, 2011, **15**, 985–1006.

12 S. Kim, S. P. Yoon, S. W. Nam, S. Hyun and S. Hong, *J. Power Sources*, 2001, **110**, 222–228.

13 P. Coddet, H. Liao and C. Coddet, *Adv. Manuf.*, 2013, DOI: 10.1007/s40436-013-0049-7.

14 C. Mansilla, J. P. Holgado, J. P. Espinos, A. R. Gonzalez-Elipe and F. Yubero, *Surf. Coat. Technol.*, 2007, **202**, 1256–1261.

15 H. J. Jong and M. C. Gyeong, *Solid State Ionics*, 2007, **178**, 1602–1607.

16 H. Hidalgo, A. L. Thomann, T. Lecas, J. Vulliet, K. Wittmann-Teneze, D. Damiani, E. Millon and P. Brault, *Fuel Cells*, 2013, **13**, 279–288.

17 M. V. F. Schlupp, A. Evans, J. Martynczuk and M. Prestat, *Adv. Energy Mater.*, 2014, **4**, 1301383.

18 S. Sanna, V. Esposito, D. Pergolesi, A. Orsini, A. Tebano, G. S. Licoccia and E. T. Balestrino, *Adv. Funct. Mater.*, 2009, **19**, 1713–1719.

19 R. Sayers, N. L. O. Flack, J. Alaria, P. A. Chater, R. G. Palgrave, S. R. C. McMitchell, S. Romani, Q. M. Ramasse, T. J. Pennycook and M. J. Rosseinsky, *Chem. Sci.*, 2013, **4**, 2403–2412.

20 I. Kosacki, C. M. Rouleau, P. F. Becher, J. Bentley and D. H. Lowndes, *Solid State Ionics*, 2005, **176**, 1319–1326.

21 N. Sakamoto, T. Inoue and K. Kato, *Cryst. Growth Des.*, 2003, **3**, 115–116.

22 Q. Xiao, H. He, S. Shao, J. Shao and Z. Fan, *Thin Solid Films*, 2009, **517**, 4295–4298.

23 Z. Feng, J. Qiang and C. Siu-Wai, *J. Appl. Phys.*, 2004, **95**, 4319–4326.

24 Y. Willinton, R. Francisca, A. C. Miguel and A. O. Jose, *J. Phys. Chem. C*, 2010, **114**, 10857–10865.

25 H. Jimenez, E. Restrepo and A. Devia, *Surf. Coat. Technol.*, 2006, **201**, 1594–1601.

26 M. I. Jones, I. R. McColl and D. M. Grant, *Surf. Coat. Technol.*, 2000, **132**, 143–151.

27 R. S. Polaki, R. Ramaseshan, F. Jose, S. Dash and A. K. Tyagi, *Int. J. Appl. Ceram. Technol.*, 2013, **10**, 45–50.

28 P. K. Dutta and H. Wilman, *J. Phys. D: Appl. Phys.*, 1970, **3**, 839–853.

29 E. Grantscharova, *Thin Solid Films*, 1993, **224**, 28–32.

30 G. Laukaitis and D. Virbukas, *Solid State Ionics*, 2013, **247**, 41–47.

31 J. P. Kar, G. Bose and S. Tuli, *Vacuum*, 2006, **81**, 494–498.

32 B. Joysurya, R. Divakar, P. J. Winterstein and C. Barry, *Appl. Surf. Sci.*, 2010, **256**, 3772–3777.

33 S. Toshio, K. Igor and U. A. Harlan, *Solid State Ionics*, 2002, **151**, 111–121.

34 V. P. Vladimir, I. K. Vladimir and L. Julie, *J. Phys. Chem. B*, 2004, **108**, 5341–5348.

35 K. Arora Akhilesh, M. Rajalakshmi, T. R. Ravindran and V. Sivasubramanian, *J. Raman Spectrosc.*, 2007, **38**, 604–617.

36 M. Guo, J. Lu, Y. Wu, Y. Wang and M. Luo, *Langmuir*, 2011, **27**, 3872–3877.

37 S. Babu, R. Thanneeru, T. Inerbaev, R. Day, A. E. Masunov, A. Schulte and S. Seal, *Nanotechnology*, 2009, **20**, 085713.

38 K. Igor, S. Toshio, U. A. Harlan and C. Philippe, *Solid State Ionics*, 2002, **149**, 99–105.

39 P. Trogadas, J. Parrondo and V. Ramani, *ACS Appl. Mater. Interfaces*, 2012, **4**, 5098–5102.

40 A. Kumar, S. Babu, A. J. Karakoti, A. Schulte and S. Seal, *Langmuir*, 2009, **25**, 10998–11007.